

# VdW Mediated Strong Magnetic Exchange Interactions in Chains of Hydrogen-Free Sublimable Molecular Qubits

Fabio Santanni,\* Matteo Briganti, Giulia Serrano, Enrico Salvadori, Alessandro Veneri, Chiara Batistoni, Sofia F. Russi, Stefano Menichetti, Matteo Mannini, Mario Chiesa,\* Lorenzo Sorace, and Roberta Sessoli\*

Cite This: *JACS Au* 2023, 3, 1250–1262

Read Online

ACCESS |

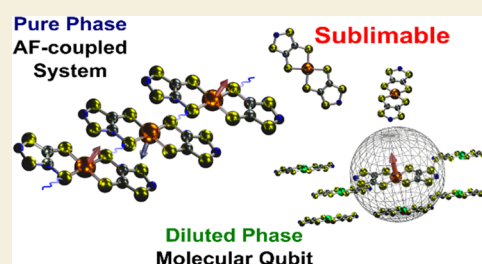
Metrics & More

Article Recommendations

Supporting Information

**ABSTRACT:** Sulfur-rich molecular complexes of dithiolene-like ligands are appealing candidates as molecular spin qubits because spin coherence properties are enhanced in hydrogen-free environments. Herein, we employ the hydrogen-free mononegative 1,3,2-dithiazole-4-thione-5-thiolate ( $\text{dttt}^-$ ) ligand as an alternative to common dinegative dithiolate ligands. We report the first synthesis and structural characterization of its  $\text{Cu}^{2+}$ ,  $\text{Ni}^{2+}$ , and  $\text{Pt}^{2+}$  neutral complexes. The XPS analysis of thermal deposition of  $[\text{Cu}(\text{dttt})_2]$  in UHV conditions indicates that films of intact molecules can be deposited on surfaces by sublimation. Thanks to a combined approach employing DC magnetometry and DFT calculations, we highlighted AF exchange interactions of  $108\text{ cm}^{-1}$  and  $36\text{ cm}^{-1}$  attributed to the two different polymorph phases. These couplings are exclusively mediated by  $\text{S}\cdots\text{S}$  VdW interactions, which are facilitated by the absence of counterions and made particularly efficient by the diffuse electron density on S atoms. Furthermore, the spin dynamics of solid-state magnetically diluted samples was investigated. The longest observed  $T_m$  is  $2.3\text{ }\mu\text{s}$  at 30 K, which significantly diverges from the predicted  $T_m > 100\text{ }\mu\text{s}$ . These results point to the diluting matrix severely affecting the coherence lifetime of  $\text{Cu}^{2+}$  species via different factors, such as the contributions of neighboring  $^{14}\text{N}$  nuclei and the formation of radical impurities in a non-completely controllable way. However, the ease of processing  $[\text{Cu}(\text{dttt})_2]$  via thermal sublimation can allow dispersion in matrices better suited for coherent spin manipulation of isolated molecules and the realization of AF-coupled VdW structures on surfaces.

**KEYWORDS:** molecular qubits, coherent spins, electron-spin resonance, magnetometry, UHV deposition, XPS spectroscopy, DFT calculations



## INTRODUCTION

Electron-spin-based quantum bits, or *qubits*, are promising platforms for implementing quantum technologies.<sup>1–3</sup> For instance, they offer the possibility of using multiple electronic and nuclear energy levels to embed logical qubits within a single object, namely, *qudits*, which is not trivial with other architectures.<sup>4–6</sup> These additional levels can be used to encode quantum error correction algorithms and improve performances.<sup>7,8</sup> The molecular approach allows for finely tuning the chemical and physical properties of the systems thanks to a targeted design.<sup>9,10</sup> The rational chemical design also allows engineering qubit–qubit interactions used to operate quantum logic gates.<sup>11–13</sup>

In contrast, spin defects in inorganic lattices<sup>1</sup> are superior in coherence times when hosted in nuclear spin-free matrices such as  $^{28}\text{Si}$  enriched crystals.<sup>14–16</sup> However, long coherence times ( $T_m$ ) approaching the *millisecond* have also been observed for specifically tailored molecular complexes. This required removing the most active nuclear spins not only from the first-coordination sphere of the central ion but also from the ligand scaffold and the matrix.<sup>17–22</sup>

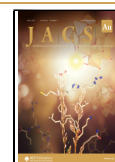
Sulfur-rich vanadium(IV) and copper(II) complexes based on dithiolene ligands are currently state-of-the-art in the molecular-spin qubits scenario.<sup>17,18,23</sup> One of the main drawbacks of employing dithiolene complexes is that they are not neutral. This feature compels to use of deuterated counterions to avoid the decoherence induced by hydrogen nuclear spins of protic cations<sup>24–26</sup> and makes the realization of nanostructures on surfaces by vacuum methods very difficult. On the contrary, neutral and sublimable molecular qubits<sup>27,28</sup> are particularly appealing for deposition on solid surfaces. This is a prerequisite for single spin addressing and manipulation through microwave pulses coupled with electric detection in STM-based nanojunctions.<sup>29–33</sup>

Received: March 16, 2023

Revised: March 31, 2023

Accepted: March 31, 2023

Published: April 13, 2023



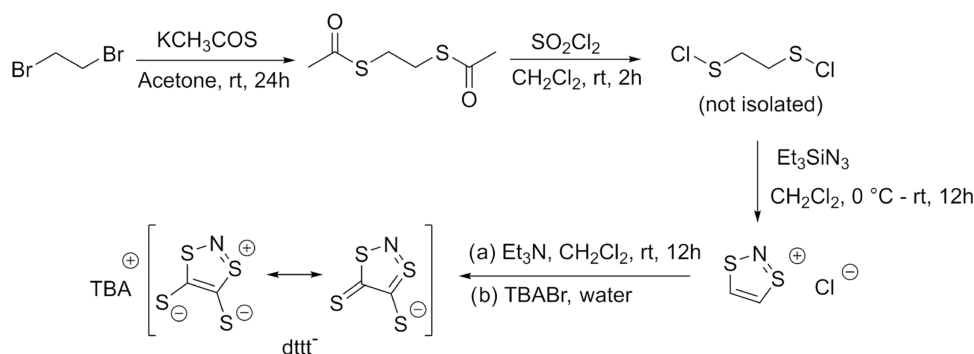


**Figure 1.** Optimized synthesis and resonance structures of TBAdttt. Only one of the symmetric resonance hybrids is reported.

Dithiolene-based complexes can be electrochemically oxidized to achieve neutral derivatives.<sup>34,35</sup> However, such an approach can hardly be employed to obtain the corresponding crystals of diamagnetic metal complexes hosting paramagnetic impurities, as requested for pulsed EPR investigations of the spin dynamics. To solve this issue, we propose here an unusual mononegatively charged sulfur-rich ligand, *i.e.*, the hydrogen-free ligand 1,3,2-dithiazole-4-thione-5-thiolate, dttt<sup>−</sup> hereafter (Figure 1),<sup>36</sup> to obtain the new copper(II) complex [Cu(dttt)<sub>2</sub>] (**1**) as a potential molecular qubit. [Cu(dttt)<sub>2</sub>] perfectly fulfills three of the essential requirements stated above for a “good” qubit: (i) the presence of a nuclear spin-depleted environment with only weakly coupled <sup>14</sup>N magnetic nuclei; (ii) the neutrality of the resulting metal complex; and (iii) good thermal stability, which is mandatory for physical vapor deposition experiments. Furthermore, we employed the dttt<sup>−</sup> ligand to synthesize two new diamagnetic complexes, *i.e.*, [Ni(dttt)<sub>2</sub>] (**2**) and [Pt(dttt)<sub>2</sub>] (**3**), to be used as diamagnetic host matrices. To our knowledge, this work is the second report on this ligand<sup>36</sup> and the first one on the corresponding M<sup>2+</sup> complexes.

Here, we report on the structural investigation of the [Cu(dttt)<sub>2</sub>] compound in the bulk phase and as a thin-film deposit obtained by thermal sublimation. We employed a combined experimental and theoretical approach to investigate and rationalize the static magnetic properties of the pure phases and the spin dynamics of diamagnetically diluted samples. The concentrated [Cu(dttt)<sub>2</sub>] compound is characterized by antiferromagnetic (AF) exchange interactions of the order of 100 cm<sup>−1</sup> along the one-dimensional network of sulfur–sulfur van der Waals (VdW) interactions, in excellent agreement with DFT predictions.

## RESULTS AND DISCUSSION

### Synthetic Strategy

The synthesis of the 1,3,2-dithiazole-4-thione-5-thiolate ligand, as a tetrabutylammonium (TBA) salt, was performed by the multistep procedure reported in Figure 1 under strict moisture- and oxygen-free conditions. The few literature reports employed gaseous chlorine to obtain the precursor (1,3,2-dithiazolium-4,5-dichloride) and, finally, the 1,3,2-dithiazolium hydrochloride salt.<sup>36–38</sup> However, in our approach, the dangerous chemical Cl<sub>2</sub> can be avoided as the closing of the heterocycle and the double bond formation is favored by the larger conjugation achieved.<sup>39</sup> Detailed experimental procedures are reported in the Supporting Information (SI) together with the spectroscopic characterization.

Metal complexes of dttt<sup>−</sup> can be easily obtained by reacting stoichiometric amounts of the ligand and the metal-salt precursor in a polar solvent (*e.g.*, MeOH, CH<sub>3</sub>CN, acetone, and pyridine).

We found that metal complexes of M<sup>2+</sup> = Cu<sup>2+</sup>, Ni<sup>2+</sup>, and Pt<sup>2+</sup> ions (compounds **1** = [Cu(dttt)<sub>2</sub>], **2** = [Ni(dttt)<sub>2</sub>], and **3** = [Pt(dttt)<sub>2</sub>]) are highly insoluble in organic solvents and not stable in organic and inorganic acids. As highlighted in the following sections, the poor solubility of this class of compounds can be correlated to their high density and strong intermolecular interactions. It follows that obtaining microcrystalline powders and single crystals suitable for structure determination is particularly challenging since products readily precipitate from polar solvents where TBAdttt is soluble. Nevertheless, microcrystalline powders of **1** and **2** containing good quality single crystals were obtained by very slow diffusion (≈2 weeks) of a MeOH solution of metal chloride salts within a pyridine solution of the ligand (see Section S1.1 of the SI). The same strategy was employed to obtain a crystalline 0.2% doped sample of **1** in **2**, *i.e.*, **2**<sub>0.2%</sub>. It was impossible to obtain single crystals of **3** using this or similar strategies.

Conversely, nanocrystalline or amorphous powders were obtained by employing different techniques, *e.g.*, by reacting the ligand and metal salts in MeOH (see Section S1.1 of the SI). We mostly used this faster synthetic method since it led to very pure products with high yields. For clarity, we will refer to the set of M<sup>2+</sup> complexes by the faster reaction in MeOH as **1**<sup>\*</sup>, **2**<sup>\*</sup>, **2**<sup>\*</sup><sub>0.2%</sub>, **2**<sup>\*</sup><sub>0.07%</sub>, **3**<sup>\*</sup>, and **3**<sup>\*</sup><sub>0.1%</sub>.

The obtained compounds were characterized by FT-IR spectroscopy (Figure S1) and elemental analysis, while the copper concentration in doped samples was confirmed by ICP-AES analysis. In addition, the thermal stability of **1** was investigated by thermogravimetric analysis (TGA). The obtained results (Figure S2) show remarkable stability up to 250 °C.

### Surface Deposition and XPS Analysis

A 20 nm thick deposit of **1** (**1-Film** hereafter) was obtained by thermal sublimation in UHV conditions on a pristine Kapton film, according to the procedure reported in Methods. The chemical composition of **1-Film** was probed by X-ray photoelectron spectroscopy (XPS) and compared with a reference bulk sample of **1** (**1-Bulk** hereafter, see Methods). Figure 2 shows the two most significant regions of interest of the XPS spectra collected on **1-Film** and **1-Bulk**, *i.e.*, the Cu 2p (left column) and S 2p (right column) core-level regions. The N 1s region is reported in Figure S3 of the SI, while the C 1s region was omitted due to contamination by air exposure. The

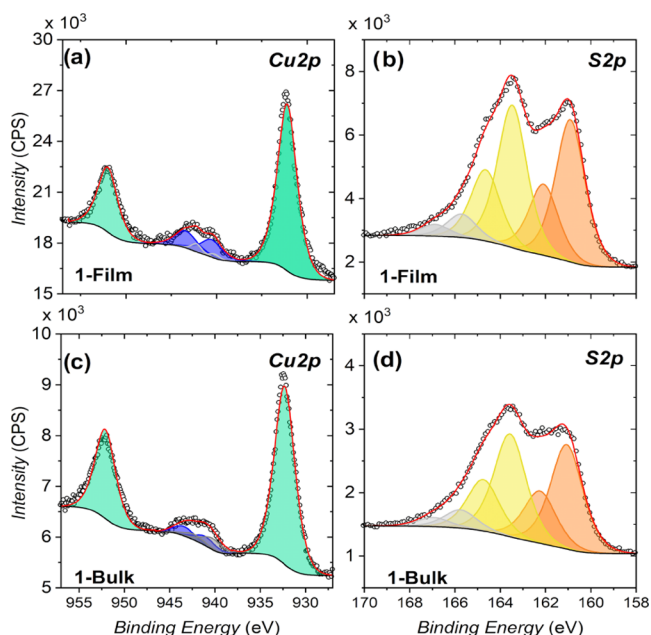


**Figure 2.** Cu 2p and S 2p regions of XPS spectra of **1-Film** on Kapton (a, b) and **1-Bulk** (c, d). The additional minor contributions at 940.2 and 942.2 eV in panels (a and c) account for the non-monochromatic X-ray source used for the experiments.

comparison between the spectral features of the two samples confirms that **1** can be deposited by thermal sublimation.

The Cu 2p XPS region (Figure 2a,c) shows two main peaks at 932.2 and 952.0 eV ascribed to the Cu 2p<sub>3/2</sub> and Cu 2p<sub>1/2</sub> spin-orbit components, respectively.<sup>40</sup> The fitted peak positions are in close agreement with those observed for the CuS<sub>4</sub> coordination environment and indicate the +2 oxidation state of the metal ion.<sup>41</sup> The peaks at 940.5 and 943.4 eV are attributed to shake-up components characteristic of the presence of Cu<sup>2+</sup> ions.<sup>42</sup> In the S 2p region (Figure 2b,d), the spectra reveal two equally intense contributions matching the stoichiometry of different S species of the ligand (*i.e.*, S–N

and S–Cu moieties, in Table S1). Each of them is characterized by two spin-orbit coupled components, *i.e.*, S 2p<sub>3/2</sub> (S–N: 163.5 eV and S–Cu: 160.9 eV) and S 2p<sub>1/2</sub> (S–N: 164.6 eV and S–Cu: 162.0 eV). The S–Cu contributions fall at lower energy with respect to the S–N ones due to the negative charge localized on the sulfur atoms (*vide infra*).<sup>43,44</sup> Additional weak signals are found at higher BE. These impurities amount to less than 8% of the total S 2p signal and can be ascribed to oxidized S species arising from air exposure.<sup>45–47</sup> The core-level XPS N 1s region is reported in Figure S3. The region is characterized by two components at 397.8 eV and 400.2 eV ascribed to the N–S moiety and shake-up components, respectively.<sup>48–50</sup> In **1-Film**, the latter is not detectable because it overlaps with the Kapton nitrogen atom signal at 397.9 eV due to the inhomogeneous coverage of the substrate.<sup>51,52</sup> The semiquantitative elemental analysis of the XPS data on the two samples shows remarkable agreement between the expected and the experimental S/Cu ratios and pinpoints the molecular integrity preservation after sublimation (see Table S11).

### Structural Characterization

Crystalline samples of **1** and **2** suitable for single-crystal X-ray diffraction were obtained following the above-described synthesis. We observed that these systems are characterized by polymorphism even within the same batch.

Two distinct phases of **1** were successfully isolated as needle- and plate-shaped single crystals. The needle-shaped ones turned out to diffract best: they belong to the C2/c space group (*n.* 15, see Table S2 of the SI) with four molecules per unit cell (Figure S4). The asymmetric unit is formed by half Cu<sup>2+</sup> ion, sitting on the inversion center, and one ligand molecule (Figure 3a). The ligand presents C1–C2 mean distance of 1.43 Å and C1–S1 and C2–S2 mean distances of 1.70 Å and 1.69 Å, respectively. Such bond lengths are in close agreement with those of dinegatively charged dithiolate copper complexes, *e.g.*, with 1,3-dithiole-2-thione-4,5-dithiolate (dtl<sup>2-</sup>) and maleonitriledithiolate (mnt<sup>2-</sup>) ligands.<sup>17,53,54</sup> It follows that the character of the C1–C2 bond is close to a C=C

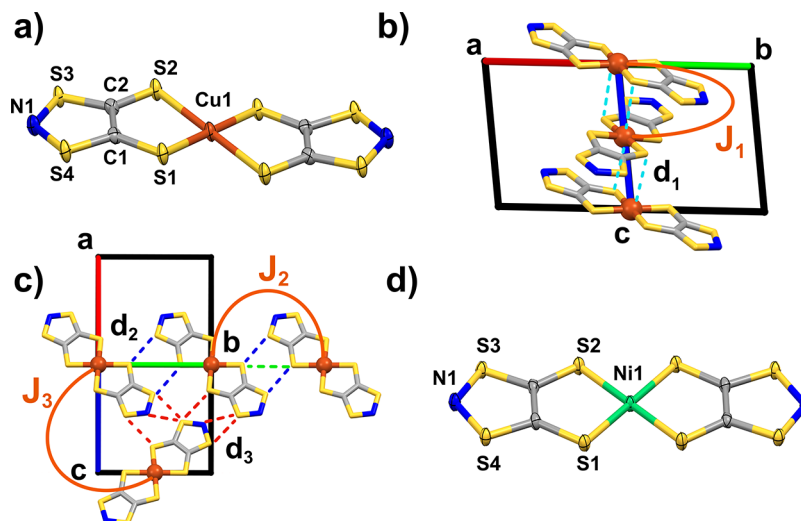


**Figure 3.** (a) Molecular structure of **1**. Atoms are reported as thermal ellipsoids at a 50% probability level. (b) View along with the perpendicular to the crystallographic direction  $[1\bar{1}0]$  of **1** (C2/c). Other molecules are omitted for clarity. (c) View along with the perpendicular to the crystallographic direction  $[101]$  of **1** (C2/c). Other molecules are omitted for clarity. (d) Molecular structure of **2**. Color code: C = gray; N = blue; S = yellow; Cu = orange; and Ni = aquamarine. Short intermolecular contacts and magnetic exchange pathways are indicated by  $d$  and  $J$ , respectively.

double bond, while C–S bonds are pretty similar to single  $\sigma$ -bonds. Thus, the two symmetric resonance hybrids (Figure 1), with two negative charges on S atoms and a positive charge in the dithiazole unit, are the most representative ones.

The Cu–S average distance (2.30 Å) and the pseudo-planar geometry, with a slight displacement of the ligands planes of 0.61 Å (Figure S5), are in line with previously reported dithiolate complexes.<sup>35,53,55</sup>

The flat molecular units form high-density crystals and tend to pile on parallel planes forming chain-like structures. The shortest Cu–Cu distance (4.15 Å) is observed between symmetry-related but magnetically nonequivalent molecules along the *c* crystallographic axis (Figure S4). The donor S atoms of neighboring molecules occupy the axial position of a strongly elongated octahedron (Figure S6) with the Cu...S' distance  $d_1 = 3.32$  Å (cyan dashed lines in Figure 3b). The peculiar stacking properties of these molecules result in a high density, similar to porphyrazine-based systems.<sup>56</sup>

It is further possible to identify a chain-like structure between molecular units lying on the same crystallographic plane, which can interact through S...S VdW interactions. Iso-oriented molecules form chains along the *b* crystallographic axis. Here, the mean Cu–Cu distance is 8.44 Å, larger than that observed in the chains along the *c*-axis. The shortest S...S distance among adjacent units is between S3...S2' atoms, *i.e.*,  $d_2 = 3.37$  Å (blue dashed lines in Figure 3c), with coordinated S atoms having S1...S2' contact at 3.89 Å (green dashed lines in Figure 3c). Secondary VdW interactions exist between S3...S3' atoms of neighboring units placed at  $d_3 = 3.60$  Å and S4...N1' at  $d_3' = 2.95$  Å (red dashed lines in Figure 2c). These interactions lead to a 2D planar structure.

A second family of crystals, plate-shaped and smaller than needle-shaped ones, was also identified in the same batch. Because of their poor crystallinity, we could not obtain an X-ray structure of this polymorph suitable for deposition in the CCDC. However, it was possible to determine its space group and general features (Figures S7 and S8 and Table S2), which will be discussed briefly below. These crystals belong to the  $P2_1/n$  space group (n. 14), with two molecules per unit cell and the asymmetric unit comprising half of the molecule. These features provide two families of magnetically nonequivalent units reported by the  $C_2$  screw axes. Thus, the molecular structure does not evidence any significant variations compared to the polymorph described above. Unlike the previous case, however, molecular units grow on stacked planes forming a 1D chain of iso-oriented molecules. The shortest Cu...Cu' distance between neighboring units of one chain is 3.87 Å, and the smallest intermolecular Cu...S' distance is  $d_1 = 3.34$  Å (Figures S8a,S8b). Secondary 1D chains are present even in this case, but the units are not coplanar. As highlighted in Figure S8b, two sets of short S–S distances can be identified, *i.e.*,  $d_2 = 3.51$  Å and  $d_3 = 3.58$  Å. Finally, we note that the two phases also occur in microcrystalline samples, as evident by comparing simulated and experimental PXRD patterns collected on **1** (Figure S10).

In analogy with the second phase of **1**, the best quality crystals of **2** present a plate-like shape. **2** crystallizes in the  $P2_1/n$  space group (No. 14, see Table S2) with two molecules per unit cell (Figure S9) and is isomorphous with the  $P2_1/n$  phase of **1**. The general features are also preserved: half Ni ion and a ligand molecule form the asymmetric unit. Molecular units of **2** present a flat and regular square-planar coordination geometry with an average Ni–S distance of 2.165 Å (Figure 3d).

Even microcrystalline powders of **2** present at least two distinct phases, as highlighted by comparing the experimental PXRD pattern to the one simulated from the  $P2_1/n$  structure (Figure S11). It was not possible to isolate crystals of the second phase suitable for X-ray structural determination, but the similarities among PXRD patterns of **1\*** and **2\*** (Figure S12) suggest that the second phase structure of **2** resembles that of **1** when crystallizing in the  $C2/c$  space group.

## Magnetism

The observed organization of molecular units in **1** might lead to strong intermolecular magnetic interactions, which prompted us to use direct current (DC) magnetometry to investigate its static magnetic properties. The measurements were performed on the microcrystalline powder sample of **1**, which contains the two different polymorphs. The  $\chi T$  vs  $T$  plot reported in Figure S14 reveals that  $\chi T$  approaches zero as the temperature decreases. This behavior highlights the presence of intermolecular antiferromagnetic (AF) exchange interactions. Similar considerations can be drawn by considering that the measured high-field  $M$  value at  $T = 2$  K (Figure S15) is far below the value of  $1 \mu_B$  expected for an ensemble of uncoupled  $S = 1/2$  centers.<sup>57</sup> Additionally, the  $M$  vs  $BT^{-1}$  curves measured at  $T = 2, 4,$  and  $8$  K are not superimposable (Figure S15).

The plot of  $\chi$  vs  $T$  is more informative, revealing a broad maximum at about 35 K (Figure 4). In the low-temperature

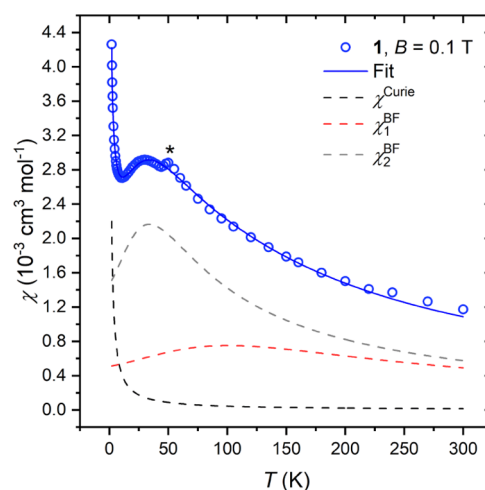


**Figure 4.** Temperature dependence of the magnetic susceptibility ( $\chi$ ) of **1**. The best-fit obtained using the Bonner–Fisher model (eq S1) is reported as a continuous line. The three contributions  $\chi^{\text{Curie}}$ ,  $\chi_1^{\text{BF}}$ , and  $\chi_2^{\text{BF}}$  in eq 1 are reported as dashed lines. The asterisk highlights an anomaly due to residual  $O_2$  impurity within the measurement chamber.

range (2–10 K), the  $\chi$  vs  $T$  curve shows the typical diverging tail due to paramagnetic impurities within an AF-coupled matrix. This contribution can be associated with defects within the crystal lattice (*e.g.*, chain truncation).

The absence of a transition to magnetic order suggests that the AF interaction is mainly confined in a 1D structure, where only short-range order can occur. We modeled the experimental  $\chi$  vs  $T$  curve using the Bonner–Fisher model developed for chains of isotropically coupled  $S = 1/2$  centers<sup>57,58</sup> and considering the presence of two crystalline phases

$$\chi = a\chi^{\text{Curie}} + (1 - a)b\chi_1^{\text{BF}} + (1 - a)(1 - b)\chi_2^{\text{BF}} \quad (1)$$

Here, the first term  $a\chi^{\text{Curie}}$  accounts for the contribution of an  $S = 1/2$  Curie's paramagnet, and the terms  $(1 - a)b\chi_1^{\text{BF}}$  and  $(1 - a)(1 - b)\chi_2^{\text{BF}}$  account for the temperature-dependent susceptibility of AF 1D spin chains (see eq S1) in the two crystalline forms. The  $a$  and  $b$  parameters are scale factors introduced to weigh the different contributions to the total  $\chi(T)$ . All the  $\chi$  terms were computed by keeping the  $g$  value fixed to 2.054, obtained by averaging the principal values of the  $g$ -tensor extracted from the CW-EPR spectra (*vide infra*). The best-fit values of isotropic exchange constants ( $\hat{H} = \sum S_i S_{i+1}$ ) are  $J = 108(6) \text{ cm}^{-1}$  and  $J' = 36(1) \text{ cm}^{-1}$ . Here,  $J$  and  $J'$  refer to the coupling in the two crystalline phases contributing similarly to the susceptibility ( $b = 0.49(3)$ ), in agreement with the PXRD pattern in Figure S10 of the SI. The extracted value of  $a = 1.11(1) \times 10^{-2}$  indicates a very small abundance of the paramagnetic impurity.

Based on the structural features presented before, different pathways for magnetic interactions can be identified in both crystallographic phases: (i) intermolecular Cu...S-Cu short contacts ( $J_1$  in Figures 3b and S8 for the  $C2/c$  and  $P2_1/n$  systems, respectively); (ii) intermolecular Cu-S...S-Cu contacts ( $J_2$  in Figures 3c and S8); (iii) intermolecular Cu-S...S(dithiazole) contact ( $J_3$  in Figures 3c and S8).

To solve this ambiguity and identify the pathway responsible for the extremely efficient coupling, we performed DFT calculations. We started from experimental crystallographic data within the broken symmetry approach (see Methods) on both structures obtained for **1**. Although path (i) presents the shortest Cu-Cu distance, only small ferromagnetic couplings were calculated,  $-3.6$  and  $-1.3 \text{ cm}^{-1}$  for the  $C2/c$  and  $P2_1/n$  structures, respectively. AF interactions of the same order of magnitude were also found for path (iii), with values of  $2 \text{ cm}^{-1}$  ( $C2/c$ ) and  $1 \text{ cm}^{-1}$  ( $P2_1/n$ ). On the other hand, stronger AF interactions were computed for path (ii), with values of  $82.1$  and  $32.7 \text{ cm}^{-1}$  for the  $C2/c$  and  $P2_1/n$  structures, respectively.

These values are in good agreement with the experimental results and allow us to attribute the best-fit parameters  $J = 108 \text{ cm}^{-1}$  and  $J' = 36 \text{ cm}^{-1}$  to the crystal phases  $C2/c$  and  $P2_1/n$ , respectively. The magnitude of the two couplings is remarkably large for intermolecular interactions mediated by VdW forces. This finding can be rationalized considering that the SOMO of **1** is a  $d_{x^2-y^2}$  orbital with antibonding character and electron density partially delocalized on the sulfur ligands. Indeed, the computed Löwdin spin density on each sulfur atom is 0.12 unpaired electrons (see Figure 5a). In the case of the short contact described as (ii), interacting molecules are coplanar and parallel, with the Cu-S...S-Cu atoms lying almost on a straight line. Such a conformation maximizes the overlap among the  $d_{x^2-y^2}$  magnetic orbitals of **1** through the sulfur atoms, which interact through the diffuse  $3p_{x/y}$  components (see Figure 5b). The unrestricted corresponding orbitals (UCO) for the broken symmetry solution clearly show a delocalization of one unpaired electron from one copper ion to the other, corresponding to another  $d_{x^2-y^2}$  orbital, which implies an AF interaction (see Figure S17). The variation in computed  $J$  magnitude from  $82.1$  to  $32.7 \text{ cm}^{-1}$  arises from the more pronounced deviation from coplanarity in the  $P2_1/n$  structure compared to  $C2/c$ . Such a deviation leads to different distances among the S2 atoms, from  $3.89 \text{ \AA}$  in the  $C2/c$  structure to  $4.24 \text{ \AA}$  in  $P2_1/n$  one.

$d_{x^2-y^2}$

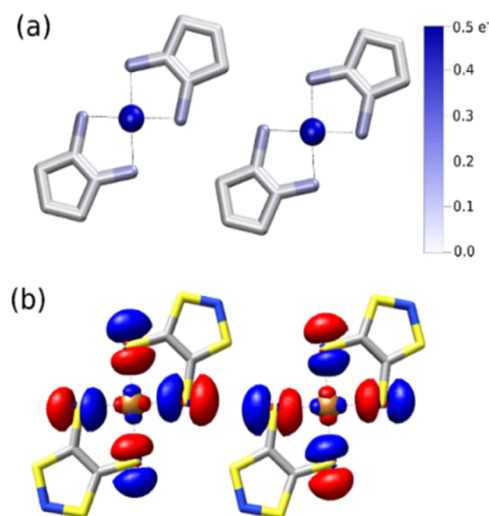


**Figure 5.** Graphical representation of calculation outcomes on dimer models of **1** for the most efficient exchange coupling pathway. (a) Computed atomic Löwdin spin density. (b) DFT computed spin-up magnetic orbital (isosurface value set to  $0.03 \text{ e}^-/\text{a}_0^3$ ). Color code: C = gray; N = blue; S = yellow; and Cu = orange.

It is worth stressing that the absence of counterions favors this close arrangement of the molecular units inside the crystal. Interestingly, a comparable VdW-mediated AF interaction,  $J \approx 100 \text{ cm}^{-1}$ , was reported for a neutral tetrathiafulvalenedithiolate copper(II) complex obtained by electrocrystallization.<sup>35</sup>

#### EPR Spectroscopy and Spin Dynamics

Continuous wave electron paramagnetic resonance (CW-EPR) spectroscopy was also used to probe the static magnetic properties of **1**. X-band ( $\nu^{\text{MW}} \approx 9.4 \text{ GHz}$ ) CW-EPR spectra of a powder sample of **1** at variable temperatures are reported in Figure 6a. The observed spectrum is typical of a square-planar  $\text{Cu}^{2+}$  ion, with axial anisotropy of the electron  $g$  factor and  $g_{\parallel} > g_{\perp} > g_e$ . The temperature dependence of the spectral intensity was analyzed by double integration of the experimental spectra. The results show a maximum at  $30 \text{ K}$ , in accordance with magnetic data (Figure S18). The experimental spectra were simulated using an anisotropic Zeeman spin Hamiltonian for an  $S = 1/2$  (see Figure S19 and Section S.7.1). The best-simulation parameters (Table S3, Figure S20) quantitatively confirmed a marked variation in the line broadening as  $T$  decreases, even highlighting a correspondence between the minimum of linewidth and the maximum of integral values. The observed line broadening could hint at the occurrence of 3D ordering at low  $T$ . Such a transition is not detectable in the magnetic measurements, where the low susceptibility of the chain is overwhelmed by the paramagnetic impurities (Figure 4).

We also successfully recorded an EPR signal at  $T = 30 \text{ K}$  (*i.e.*, in correspondence to the  $\chi$  maximum) on **1-Film** (Figure S21 of SI). Here, the signal intensity is markedly reduced by the low number of spins ( $\approx 3.4 \times 10^{14}$  spins, according to the molecular density of **1** in the  $C2/c$  phase), close to the sensitivity limit.<sup>39</sup> The similarity of the spectra, though significantly broader in **1-Film**, confirm that the molecular integrity and magnetic properties are maintained even on the surface.

X-band CW-EPR experiments on solid magnetic dilutions  $2_{0.2\%}$  and  $2^*_{0.2\%}$  (see PXRD patterns in Figure S12) were performed (see Methods). The comparison of the two spectra

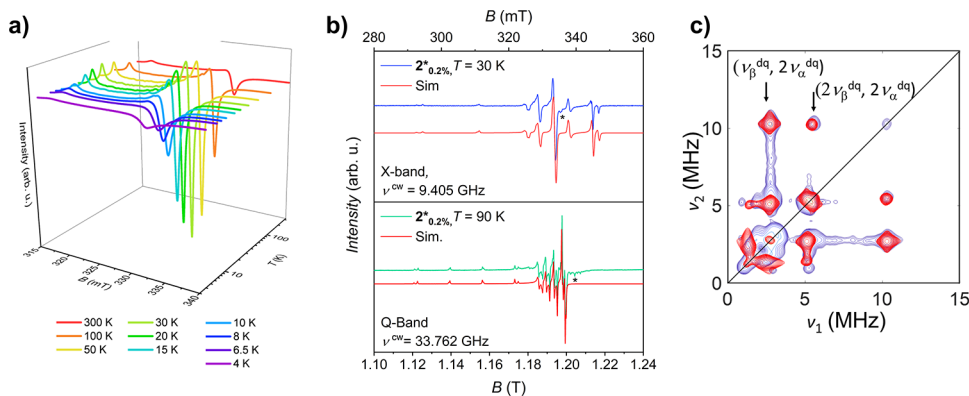


**Figure 6.** (a) X-band CW-EPR spectra collected at different temperatures on a powder sample of **1**. Spectra are rescaled by considering the mw power and receiver gain levels. (b) Plot of experimental and simulated X- and Q-band spectra of **2**<sub>0.2%</sub>. Simulated spectra are reported as solid red lines. The asterisk around 1.21 T highlights the presence of paramagnetic impurities dispersed within the batch. (c) X-band HSCORE spectrum collected on **2**<sub>0.2%</sub> at 306.7 mT. Simulated curves are reported as red traces.

(Figure S22) revealed a better-resolved structure for **2**<sub>0.2%</sub>, whose spectrum at  $T = 30$  K is reported in Figure 6b. It reveals the typical hyperfine features of  $\text{CuS}_4$  systems in a distorted square-planar geometry,<sup>60</sup> where the splitting of the lines is due to the two  $I = 3/2$  Cu isotopes ( $^{63}\text{Cu}$ ,  $I = 3/2$ , natural abundance,  $NA = 69.17\%$ ;  $^{65}\text{Cu}$ ,  $I = 3/2$ ,  $NA = 30.83\%$ ). Q-band ( $\nu^{\text{MW}} \approx 34$  GHz) CW (Figure 6b) and echo-detected field swept (EDFS) EPR spectra (Figure S23) were then recorded. These show a better-resolved spectral structure in agreement with the X-band data. Experimental spectra were simulated<sup>61</sup> by employing the following spin Hamiltonian

$$\hat{H}_S = \mu_B \vec{B} \cdot \hat{g} \cdot \hat{S} + \hat{I} \cdot \hat{A}^{\text{Cu}} \cdot \hat{S} + (\hat{I}^{\text{N}} + \hat{I}^{\text{N}'}) \cdot \hat{A}^{\text{N}} \cdot \hat{S} \quad (2)$$

where  $\mu_B$  is the Bohr magneton,  $\vec{B}$  is the applied magnetic field,  $\hat{I}$  and  $\hat{S}$  are the nuclear and electron-spin operators for the  $\text{Cu}^{2+}$  ion, respectively,  $\hat{A}^{\text{Cu}}$  is the hyperfine coupling tensor, and  $\hat{A}^{\text{N}}$  is the hyperfine coupling tensor accounting for the interaction between the metal ion and the two equivalent  $^{14}\text{N}$  nuclear spins. The set of best parameters extracted from our computer simulation of X- and Q-band spectra is reported in Tables 1 and S4. The relatively small  $g_z$  and  $^{\text{Cu}}A_z$  values

**Table 1. Best-Fit Parameters Extracted from the X- and Q-Band CW Spectra Simulations of **2**<sub>0.2%</sub>**<sup>a</sup>

	computed	experimental
$g_x$	2.0266	2.0213(3)
$g_y$	2.0291	2.0246(6)
$g_z$	2.1025	2.1015(1)
$^{\text{Cu}}A_x^b$	-83	112(2)
$^{\text{Cu}}A_y^b$	-84	115(2)
$^{\text{Cu}}A_z^b$	-531	496(3)
$^{\text{N}}A_x^b$	-0.08	3.0(5)
$^{\text{N}}A_y^b$	0.85	2.6(5)
$^{\text{N}}A_z^b$	-2.01	2.6(5)

<sup>a</sup>Values of  $^{\text{N}}A_x$ ,  $^{\text{N}}A_y$ , and  $^{\text{N}}A_z$  were extracted from X-band HSCORE experiments on the same sample by adopting an axial approximation. Spectra simulations were performed assuming the same reference frame for  $\hat{g}$ ,  $\hat{A}^{\text{Cu}}$ , and  $\hat{A}^{\text{N}}$ . The computed tensors are consistently almost collinear, with largest Euler angle  $\approx 10^\circ$  (reference frame:  $z$  perpendicular to the  $\text{CuS}_4$  plane and  $x$  along the Cu-N direction).

<sup>b</sup>Hyperfine tensor components are given in MHz, and only their absolute value is experimentally determined.

compared to oxo-Cu complexes<sup>62</sup> are indicative of the delocalization from the  $d_{x^2-y^2}$  orbital of copper onto the sulfur  $p$ -orbital.<sup>63</sup> This concurs with the small distortion of the first-coordination sphere discussed above (see the Structural Characterization section) to the slight rhombicity of the Cu magnetic tensors. Moreover, the  $g_z/{}^{\text{Cu}}A_z$  ratio agrees with that observed in other  $\text{CuS}_4$  systems with a square-planar geometry and axial symmetry (see Figure S24).<sup>60,64</sup>

In order to map the degree of delocalization of the wave function, HSCORE experiments were performed at X-band and different magnetic field settings to determine the hyperfine coupling interaction with the two distal  $^{14}\text{N}$  nuclei (Figure S27, Table S6). The HSCORE spectrum of **2**<sub>0.2%</sub> collected at a magnetic field corresponding to the  $m_I = -3/2$  EPR transition (306.7 mT) is reported in Figure 6c. The spectrum is characterized by a series of cross-peaks in both quadrants (Figure S27b), assigned to the hyperfine interaction of the unpaired electron with two equivalent  $^{14}\text{N}$  nuclei ( $I = 1$ ). The most intense cross-peaks are centered at about (2.8, 5.6) MHz and (5.6, 2.8) MHz. An equivalent pair of cross-peaks is observed as a mirror image in the (+, -) quadrant. These peaks are assigned to the double-quantum ( $dq$ ) nuclear frequencies ( $\Delta m_I = 2$ ) arising from the hyperfine interaction of the unpaired electron with a single  $^{14}\text{N}$  nucleus. In addition, lower intensity cross-peaks are observed in both quadrants at approximately  $| (2, 8), (11.2) |$  MHz and in the (+, +) quadrant at (5.6, 11.2) and (11.2, 5.6) MHz. These transitions correspond to combinations of the form  $(\nu_\beta^{\text{dq}}, 2\nu_\alpha^{\text{dq}})$  and  $(2\nu_\beta^{\text{dq}}, \nu_\alpha^{\text{dq}})$ , which can only be observed if two equivalent  $I = 1$  nuclei (*i.e.*, two equivalent  $^{14}\text{N}$  nuclei) are coupled to the electron spin. This assignment is corroborated by computer simulations performed at different magnetic field settings, which provide the full nitrogen hyperfine and quadrupole tensors (see Section S.7.3).

The spin Hamiltonian parameters were also computed by DFT on the X-ray-derived geometry of the isolated molecule. The agreement with the simulated  $g$ -tensor and Cu hyperfine coupling constants (see Table 1) is excellent. Discrepancies are found for the nitrogen hyperfine coupling tensor. Although the largest computed hyperfine component ( $-2.01$  MHz) is consistent with the absolute value determined from HSCORE (3 MHz), the isotropic contact contribution ( $-0.42$  MHz) is significantly smaller compared to the experimental one (2.7 MHz). The significant role played by intermolecular

interactions due to the close packing might reduce the accuracy of the isolated molecule model employed in our calculations.

Inversion recovery and echo decay experiments were performed at Q-band frequency and  $B = 1.20$  T (corresponding to the maximum in the EDFS spectrum) to obtain information on the temperature dependence of the spin-lattice relaxation time  $T_1$  and the coherence time  $T_m$ , respectively. The obtained echo traces (Figure S28) are fitted with a stretched exponential model,<sup>65</sup> and the extracted  $T_m$  and  $T_1$  values are reported in Figure 7a (values are reported in Table

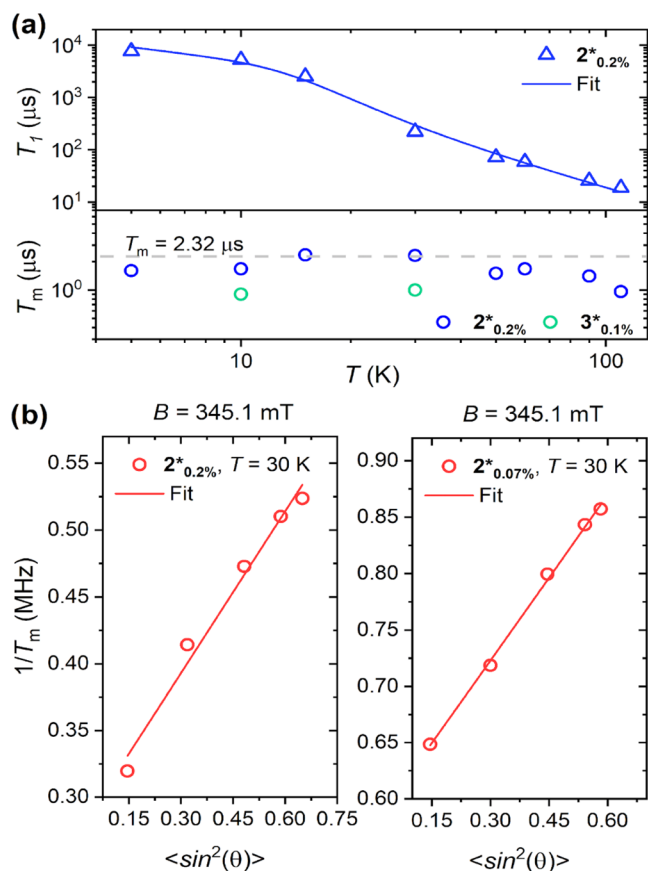


**Figure 7.** (a) Temperature dependence of  $T_1$  and  $T_m$  on solid doped samples  $2^*_{0.2\%}$  and  $3^*_{0.1\%}$  extracted from Q-band inversion recovery and Hahn-echo experiments at  $B = 1.20$  T. The fit of the  $T_1$  trend is reported as a solid line. Error bars are within the size of the symbols. (b) Dephasing rate values  $1/T_m$  of  $2^*_{0.2\%}$  and  $2^*_{0.07\%}$  at 30 K as a function of  $\langle \sin^2 \theta \rangle$  determined at 345.1 mT and X-band frequency.

S7) as a function of temperature. The temperature dependence of  $T_1$  follows the trend expected for an  $S = 1/2$  system.<sup>21,66,67</sup> Below  $T = 10$  K,  $T_1$  is only weakly temperature dependent, suggesting a dominant direct relaxation process. Above 10 K, the temperature dependence  $T$  is markedly increased, leading to a fast drop in relaxation times. This behavior can be correlated to the activation of some vibrational modes that lead to a second-order (Raman) relaxation process. The experimental results are indeed perfectly reproduced through the fit implemented with the model in eq 3.<sup>68</sup>

$$T_1^{-1} = a_{\text{dir}} \frac{e^{(\Delta E/k_B T)}}{(e^{(\Delta E/k_B T)} - 1)} + a_{\text{Ram}} \frac{e^{(\hbar\omega/k_B T)}}{(e^{(\hbar\omega/k_B T)} - 1)^2} \quad (3)$$

where the first term models the direct process (here,  $\Delta E = 1.1$   $\text{cm}^{-1}$  is fixed to the Zeeman splitting), and the second accounts for the Raman process promoted by an optical mode of frequency  $\hbar\omega = 54(10)$   $\text{cm}^{-1}$ . The two terms are rescaled by two weight constants  $a_{\text{dir}} = 2.9(5) \times 10^{-8}$  Hz and  $a_{\text{Ram}} = 3.0(8) \times 10^{-5}$  Hz, respectively. All the extracted values are comparable to those observed in other rigid heterocyclic  $\text{Cu}^{2+}$  complexes.<sup>21</sup> The  $T_m$  values show an almost temperature-independent trend up to 100 K. The highest value of  $T_m = 2.32$   $\mu\text{s}$  is observed at 30 K, which gradually decreases below 1  $\mu\text{s}$  at the highest measured temperature. This is analogous to what has been previously observed in other solid dilutions of  $\text{Cu}^{2+}$  complexes.<sup>21,69,70</sup>

The measured  $T_m$  value deserves some comment. The loss of phase memory in solid samples stems from stochastic processes producing relaxation in the spin system. All the relaxation mechanisms are due to the time fluctuations of the magnetic parameters, such as the hyperfine or electron–electron dipolar interactions. The time modulations of dipolar interactions result from the motions of the paramagnet in the solid matrix (modifying the dipolar tensors) and from the flipping of the spins (reversing the sign of the dipolar interaction).<sup>71</sup>

In the present case, a source of dephasing can be the presence of hyperfine interactions with  $^{14}\text{N}$  ( $I = 1$ ) nuclei. Their effect on  $T_m$  can be estimated by an analytical model which makes use of the experimentally determined hyperfine coupling constants (Table 1).<sup>22,67,72</sup> Neglecting the hyperfine interaction with neighboring molecules (see Methods), the resulting  $T_m$  value obtained by this model is 324  $\mu\text{s}$ . This value exceeds the experimentally measured  $T_m$  by ca. two orders of magnitude. The experimental  $T_m$  values are also significantly shorter than those observed for  $[\text{Cu}(\text{mnt})_2]^{2-}$ ,<sup>17</sup> for which the Cu–N hyperfine dipolar coupling was considered irrelevant, while they are comparable to those reported for porphyrin and porphyrazine ligands exhibiting Cu–N coupling constants of about 50 MHz.<sup>21,67</sup> This inconsistency suggests that other sources of decoherence are present.

We, therefore, consider the effect of the electron–electron dipolar interaction, which depends on the distances between electron spins and, consequently, on their local concentration. Spin flips due to stochastic  $T_1$  or  $T_2$  relaxation processes are intrinsically present and produce the spin diffusion phenomenon. However, spin flips can also be artificially produced by the microwave pulses themselves, and their effect, in this case, is called instantaneous diffusion.<sup>73</sup> An estimate of the “true”  $T_m^*$  (spin diffusion) can thus be obtained if the contribution of instantaneous diffusion to the spin dephasing rate,  $1/T_m$ , is assessed. To achieve this, we measured coherence times as a function of the refocusing pulse turning angle,  $\theta$ , by varying the applied microwave power (see Figure 7b and Section S.7.5).<sup>71,74</sup> The so-determined phase memory times ( $T_m^*$ ) for  $2^*_{0.2\%}$  are only about two times longer than the  $T_m$  values obtained via standard echo decay measurements (Figure S29), indicating a weak effect of instantaneous diffusion. By considering the crystallographic structure of **2** and the 0.2% Cu doping level, a concentration of  $\approx 7.6 \times 10^{18}$  spins/ $\text{cm}^3$  is derived. Assuming a random distribution (consistent with the small instantaneous diffusion effect), a mean spin–spin distance of  $\sim 5$  nm is extracted, corresponding to a dipolar coupling frequency of 0.4 MHz and an upper  $T_m$  limit of  $\sim 2.5$   $\mu\text{s}$ . The modest increase in  $T_m$  by suppressing spin–spin

instantaneous diffusion suggests that additional decoherence mechanisms are active.

To increase the mean spin–spin distance and reduce spin flip-induced decoherence, we hence extended the investigation to a 0.07% doped sample,  $2^*_{0.07\%}$  (PXRD reported in Figure S12 of the SI). However, we find that increasing the Cu dilution makes the contribution of the paramagnetic impurities more relevant, further complicating the EPR spectrum and  $T_m$  determination. The dominant paramagnetic impurity formed during the synthesis was characterized by recording  $T_1$ -filtered spectra (see Section S7.2.2, Figures S25–S26, and Table S5).  $T_m$  measured as a function of the refocusing pulse angle is reported in Figure 7b, while the temperature dependence is reported in Figure S29. The results indicate that no improvement is achieved by increasing the dilution.

Changing the diamagnetic host from Ni to Pt in  $3^*_{0.1\%}$  to avoid spurious EPR silent  $S = 1$  species formed by the axial coordination of the Ni ions did not improve the coherence properties (see Figure 7). In addition, the investigation of more crystalline  $2^*_{0.2\%}$  revealed similar  $T_m$  values (Figure S23), suggesting that the amorphous character of  $2^*_{0.2\%}$  is irrelevant. This thorough analysis shows that several factors intrinsically linked to the nature of the diluting matrix, such as the contributions of neighboring  $^{14}\text{N}$  nuclei and the formation of radical impurities, limit the coherence lifetime of diluted  $\text{Cu}^{2+}$  species in this system. Nevertheless, the possibility of coherent manipulation of spins in  $2^*_{0.2\%}$  is demonstrated by the detection of the linear dependence of Rabi oscillation frequencies ( $\Omega_R$ ) on the  $B_1$  microwave field (Figure 8 and Methods)

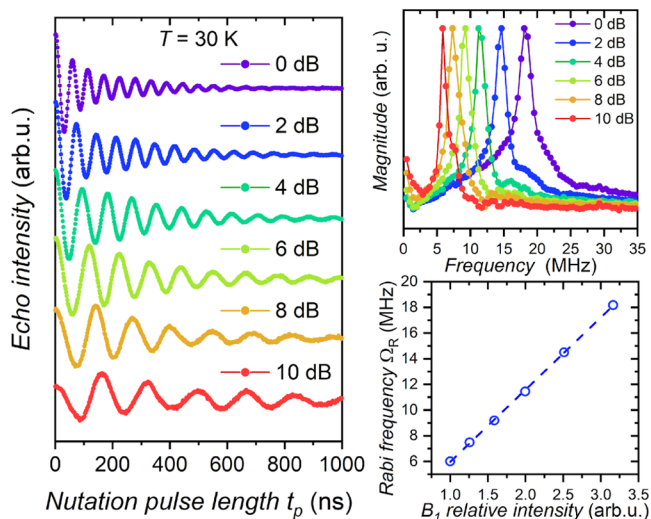


**Figure 8.** Rabi oscillations at different attenuation values of pulses collected from nutation experiments on  $2^*_{0.2\%}$ . In the top right corner, Fourier transform (FT) of nutation experiments. In the bottom right corner, the FT maxima coordinate ( $\Omega_R$ ) plotted as a function of the  $B_1$  relative intensity. A dashed line is added to highlight the linear trend.

Furthermore, the thermal stability and sublimation properties of **1** can be exploited to obtain isolated  $\text{Cu}^{2+}$  sites in different matrixes or on a surface, thus circumventing the matrix limitations.

## CONCLUSIONS

In summary, by employing the almost unexplored hydrogen-free  $\text{dttt}^-$  ligand, we successfully synthesized and characterized for the first time three neutral  $M^{2+}$  complexes and validated their suitability for surface deposition experiments through thermal sublimation in UHV conditions by XPS, hence identifying a promising new example of a processable qubit.

Thanks to the diffuse electron density on the sulfur atoms and the absence of the counterion, the concentrated phase of the copper derivative exhibits AF exchange interactions reaching  $100\text{ cm}^{-1}$  between VdW interacting molecules. DFT calculations allowed the identification of the exchange pathway and the rationalization of the significant differences between the investigated polymorphs. By combining the peculiar magnetic properties of **1** with its excellent processability by the vapor phase, the system can be employed for different applications based on nanostructured surfaces, e.g., for developing spintronic devices based on AF-coupled 2D molecular materials. In this respect, new experiments aimed at investigating the patterning and magnetic properties of **1** once deposited on surfaces are currently on the way.

On the other hand, the availability of the diamagnetic Ni and Pt analogues allowed us to investigate the coherent spin dynamics of diluted samples. The predicted  $T_m$  should exceed  $100\ \mu\text{s}$  and outperform the dithiolenic complex  $(\text{P}(d_5\text{-Ph})_4)[\text{Cu}(\text{mnt})_2]$ , which holds the record  $T_m$  for molecular spin qubits in the crystalline phase.<sup>17</sup> However, the same factors that favor strong exchange coupling interactions in such planar and conjugated structures (stacking and VdW interactions) reduce the solubility of this family of compounds almost to zero. Therefore, fine control of the homogeneity of solid dilutions is prohibitive and poorly reproducible. As a result, the obtained doped samples are characterized by coherence properties that do not reach the expected values of hundreds of  $\mu\text{s}$ . Additional contributions to decoherence might arise from the nuclear nitrogens bath and radical impurities present in the diamagnetic hosts. Nonetheless, the ease of processability via thermal sublimation might be used to disperse **1** in more suitable matrices. The flat structure makes **1** an ideal candidate for single-spin experiments of coherent manipulation through combined EPR–STM approaches.<sup>30–32</sup>

## METHODS

### Film Preparation

The film preparation of **1** on Kapton was carried out under UHV conditions ( $\approx 7 \times 10^{-8}$  mbar) in a custom sublimation chamber. **1** powders were heated by the Joule effect in a quartz crucible using a tungsten filament, and a thermocouple in direct contact with the crucible was used to monitor the temperature. The powders were preliminarily degassed at  $150\text{ }^\circ\text{C}$  in UHV for 24 h. During deposition, the crucible was heated up to the sublimation temperature of about  $200\text{ }^\circ\text{C}$ . Before starting the deposition, the 20 nm thick deposit was calibrated by monitoring the molecular flux by a quartz microbalance (QCM). The QCM and the Kapton substrate were positioned at about 5 cm from the quartz crucible. The Kapton substrate was employed as pristine, and its surface was not treated with chemicals.

### XPS Analysis

X-ray photoelectron spectroscopy (XPS) was carried out in a UHV chamber with a base pressure lower than  $10^{-9}$  mbar. The chamber was equipped with nonmonochromatized Al  $K_\alpha$  radiation ( $h\nu = 1486.6\text{ eV}$ ) and a hemispherical electron/ion energy analyzer (VSW mounting a 16-channel detector). During operation, the X-ray source was set at 12 kV and 11 mA, and photoelectrons were collected



normally to the sample surface, maintaining the angle between the analyzer and X-ray source fixed at 54.5°. XPS spectra were acquired by a fixed analyzer transmission mode with a pass energy of 44.0 eV. The components of the XPS spectra were analyzed by the CasaXPS software. A Shirley function was used to fit the background, and the components were fitted by a combination of Gaussian and Lorentzian functions (60:40). All spectra were calibrated according to the adventitious carbon signal at 284.5 eV, as reported in the literature.<sup>75</sup> The semiquantitative elemental analysis was performed by employing the cross-section values extracted from the literature<sup>76</sup> and removing the carbon contribution that was affected by air contamination during sample manipulation.

### Single-Crystal X-ray Characterizations

Single-crystal X-ray diffraction experiments were performed on a Bruker Kappa APEX-II DUO diffractometer using both Cu K $\alpha$  ( $\lambda = 1.542 \text{ \AA}$ ) and Mo K $\alpha$  radiations ( $\lambda = 0.7107 \text{ \AA}$ ). The crystal was kept at 100.0 K during data collection. The structures were solved employing the Olex2 software package<sup>77</sup> by the intrinsic phasing method (SHELXT).<sup>78</sup> The refinement was carried out using a full matrix least-squares minimization method (SHELXL package).<sup>79</sup> All non-H atoms were refined with anisotropic displacement parameters. The graphical material was prepared using Mercury CSD 2022.2.0 (copyright CCDC, <http://www.ccdc.cam.ac.uk/mercury/>).<sup>80</sup> A summary of the crystallographic data and the structure refinement for compounds **1** and **2** are reported in Table S2.

Complete crystallographic data for the solved structures have been deposited in the Cambridge Crystallographic Data Centre with CCDC numbers 2220029 (**1**) and 2220030 (**2**), respectively.

### Magnetic Measurements

Direct current magnetic measurements were performed in the  $T$  range 2–300 K ( $B = 0.1 \text{ T}$ ) or in the  $B$  range 0–5 T ( $T = 2, 4, 8 \text{ K}$ ) using a quantum design magnetic properties measuring system (QD-MPMS) equipped with a superconductive quantum interference device (SQUID). Magnetization data were corrected for the sample holders previously measured using the same conditions and for the diamagnetic contributions as deduced by using Pascal's constant tables.<sup>81</sup>

### Theoretical Calculations Details

All the calculations were performed with the ORCA 5.0.2 quantum chemistry package.<sup>82</sup> The X-ray structure of **1** and **2** were employed without any further geometry optimization. The intermolecular exchange interaction was computed in dimer models. The models were made using two molecular units extracted from the crystal structure. The PBE0 hybrid exchange-correlation functional was chosen.<sup>83</sup> The basis set def2-TZVPP was employed for all atoms.<sup>84</sup> The broken symmetry (BS) approach was used to extract the magnetic-coupling constants.<sup>85</sup> Single-point calculations on both the triplet and the broken symmetry state were performed. Hence, within the Heisenberg Hamiltonian  $H_{\text{HDVV}} = J S_1 \cdot S_2$ , the value of the exchange constant was computed within the following formula

$$J = (E_{\text{HS}} - E_{\text{BS}})/(2S_1 S_2)$$

where HS is the triplet ( $S = 1$ ) and BS is the broken symmetry state. The use of Yamaguchi's expression provides the same results ( $J = 81.8 \text{ cm}^{-1}$  and  $J' = 32.7 \text{ cm}^{-1}$ ).<sup>86</sup>

The calculation of single-ion spin Hamiltonian parameters, *i.e.*,  $g$ -tensor and hyperfine coupling, was performed at the DFT level of theory with the PBE0 functional on the single-molecule X-ray structure of **1**. The Aug-cc-pVTZ-J basis set has been employed.<sup>87</sup> The RIJCOSX approximation was applied with the default grid integration accuracy as implemented in ORCA.<sup>88</sup>

The coherence times at the single-molecule level have been estimated using the calculated and experimental values of the hyperfine coupling constants. The nitrogen's nuclei contributions to the coherence time have been computed on the basis of previous works.<sup>22,67,89</sup> Within this approach,  $T_m = \Delta/(E_n)^2$ , where  $E_n$  is the nuclear contribution to the echo linewidth and  $\Delta$  is the value of the

gap between the two qubit states (33.3 GHz here).  $E_n$  can be computed within the following formula

$$E_n^2 = \sum_k \frac{(\omega_k^{\parallel})^2 I_k (I_k + 1)}{3} \quad (4)$$

where  $\omega_k$  is the difference between the interaction of the electronic spin with the  $k$ th active nuclear spin when the electronic spin is in two different states.

### Electron Paramagnetic Resonance Spectroscopy

CW X-band EPR spectra of all samples were recorded on a Bruker Elexsys E500 spectrometer equipped with an SHQ cavity ( $\nu = 9.43 \text{ GHz}$ ). Low-temperature measurements were obtained using an Oxford Instruments ESR900 continuous-flow helium cryostat. Thick film measurements were performed using a goniometer equipped with a plastic crystal holder. The residual signal of the crystal holder was collected in the same experimental conditions and subtracted from that of the molecular film.

Pulse EPR measurements at X- (9.73 GHz) and Q-band (33.8GHz) frequencies were collected on a Bruker ElexSys E580 spectrometer equipped with dielectric ring resonators (EN 4118X-MD4 and EN 5107D2) housed in an Oxford Instruments cryostat CF 935.

$T_m$  measurements were performed using a two-pulse Hahn spin echo sequence,  $\pi/2 - \tau - \pi - \tau - \text{echo}$ , and varying the interpulse delay  $\tau$  from an initial value of 120 ns with time increments of 8 ns for 821 points; the  $\pi/2$  and  $\pi$  lengths were set to 16 and 32 ns, respectively.  $T_m$  measurements employing different turning angles were implemented by adjusting the microwave attenuation without changing the pulse timings.

$T_1$  measurements were performed through the inversion recovery pulse sequence,  $\pi - T - \pi/2 - \tau - \pi - \tau - \text{echo}$ , where the interpulse delay  $T$  has an initial value of 1000 ns,  $\pi/2$  and  $\pi$  have a length of 16 and 32 ns, respectively, and  $\tau$  is fixed to 400 ns. The time increments of  $T$  and the shot repetition rate were adjusted at each temperature.

Rabi oscillations were collected using the pulse sequence,  $\pi_{\text{RABI}} - T - \pi/2 - \tau - \pi - \tau - \text{echo}$ , where the  $\pi_{\text{RABI}}$  pulse was incremented from 2 to 3196 ns in steps of 4 ns (800 points),  $\pi/2$  and  $\pi$  had a length 16 and 32 ns, respectively, and  $\tau$  was fixed at 400 ns. Experiments were performed at  $T = 80 \text{ K}$ , while the microwave amplifier attenuation was varied in steps of 3 dB, from 0 to 9 dB. The experimental time traces were baseline corrected with a zeroth order polynomial and Fourier transformed to yield the characteristic Rabi frequency.

X-band hyperfine sublevel correlation (HYSCORE) experiments were performed with the pulse sequence  $\pi/2 - \tau - \pi/2 - t_1 - \pi - t_2 - \pi/2 - \tau - \text{echo}$ , applying a four-step phase cycle for deleting unwanted echoes.<sup>90</sup> Pulse lengths of  $t_{\pi/2} = 16 \text{ ns}$  and  $t_{\pi} = 16 \text{ ns}$  and a shot repetition rate of 0.5 kHz were used. The increment of the time intervals  $t_1$  and  $t_2$  was 20 ns, starting from 100 ns with a data matrix of  $170 \times 170$ ; the pulse delay  $\tau$  value was set to 140 ns. The time traces of HYSCORE spectra were baseline-corrected with a third-order polynomial, apodized with a hamming window, and zero-filled to 2048 points. After the 2D Fourier transformation, the absolute-value spectra were calculated.

All the EPR spectra were simulated by using the Easyspin package (version 6.0.0 dev 26).<sup>61</sup>

## ASSOCIATED CONTENT

### Supporting Information

The Supporting Information is available free of charge at <https://pubs.acs.org/doi/10.1021/jacsau.3c00121>.

Additional information about synthesis, materials, and methods; UV-vis, TGA, FT-IR, XPS, and PXRD results; additional information about the crystallographic structural characterization; more information about the **1**  $P2_1/n$  crystal structure; additional information about models and magnetometry characterization of **1** and **2**;

additional information about EPR spectra simulations; and additional pulsed EPR experiments (PDF)

Crystallographic data 1 (CIF)

Crystallographic data 2 (CIF)

## AUTHOR INFORMATION

### Corresponding Authors

**Fabio Santanni** – Dipartimento di Chimica “Ugo Schiff” - DICUS, Università degli Studi di Firenze, I-50019 Sesto Fiorentino, Firenze, Italy; Consorzio Interuniversitario Nazionale di Scienza e Tecnologia dei Materiali - INSTM, I-50121 Firenze, Italy; [orcid.org/0000-0002-0506-8333](https://orcid.org/0000-0002-0506-8333); Email: [Fabio.Santanni@unifi.it](mailto:Fabio.Santanni@unifi.it)

**Mario Chiesa** – Consorzio Interuniversitario Nazionale di Scienza e Tecnologia dei Materiali - INSTM, I-50121 Firenze, Italy; Dipartimento di Chimica e NIS Centre, Università di Torino, I-10125 Torino, Italy; [orcid.org/0000-0001-8128-8031](https://orcid.org/0000-0001-8128-8031); Email: [Mario.Chiesa@unito.it](mailto:Mario.Chiesa@unito.it)

**Roberta Sessoli** – Dipartimento di Chimica “Ugo Schiff” - DICUS, Università degli Studi di Firenze, I-50019 Sesto Fiorentino, Firenze, Italy; Consorzio Interuniversitario Nazionale di Scienza e Tecnologia dei Materiali - INSTM, I-50121 Firenze, Italy; [orcid.org/0000-0003-3783-2700](https://orcid.org/0000-0003-3783-2700); Email: [Roberta.Sessoli@unifi.it](mailto:Roberta.Sessoli@unifi.it)

### Authors

**Matteo Briganti** – Dipartimento di Chimica “Ugo Schiff” - DICUS, Università degli Studi di Firenze, I-50019 Sesto Fiorentino, Firenze, Italy; Consorzio Interuniversitario Nazionale di Scienza e Tecnologia dei Materiali - INSTM, I-50121 Firenze, Italy; [orcid.org/0000-0001-8576-3792](https://orcid.org/0000-0001-8576-3792)

**Giulia Serrano** – Consorzio Interuniversitario Nazionale di Scienza e Tecnologia dei Materiali - INSTM, I-50121 Firenze, Italy; Dipartimento di Ingegneria Industriale - DIEF, Università degli Studi di Firenze, I-50139 Firenze, Italy; [orcid.org/0000-0001-7953-7780](https://orcid.org/0000-0001-7953-7780)

**Enrico Salvadori** – Consorzio Interuniversitario Nazionale di Scienza e Tecnologia dei Materiali - INSTM, I-50121 Firenze, Italy; Dipartimento di Chimica e NIS Centre, Università di Torino, I-10125 Torino, Italy; [orcid.org/0000-0003-4394-9438](https://orcid.org/0000-0003-4394-9438)

**Alessandro Veneri** – Dipartimento di Chimica “Ugo Schiff” - DICUS, Università degli Studi di Firenze, I-50019 Sesto Fiorentino, Firenze, Italy; Consorzio Interuniversitario Nazionale di Scienza e Tecnologia dei Materiali - INSTM, I-50121 Firenze, Italy

**Chiara Batistoni** – Consorzio Interuniversitario Nazionale di Scienza e Tecnologia dei Materiali - INSTM, I-50121 Firenze, Italy

**Sofia F. Russi** – Dipartimento di Chimica e NIS Centre, Università di Torino, I-10125 Torino, Italy

**Stefano Menichetti** – Dipartimento di Chimica “Ugo Schiff” - DICUS, Università degli Studi di Firenze, I-50019 Sesto Fiorentino, Firenze, Italy; Consorzio Interuniversitario Nazionale di Scienza e Tecnologia dei Materiali - INSTM, I-50121 Firenze, Italy; [orcid.org/0000-0001-6745-7484](https://orcid.org/0000-0001-6745-7484)

**Matteo Mannini** – Dipartimento di Chimica “Ugo Schiff” - DICUS, Università degli Studi di Firenze, I-50019 Sesto Fiorentino, Firenze, Italy; Consorzio Interuniversitario Nazionale di Scienza e Tecnologia dei Materiali - INSTM, I-50121 Firenze, Italy; [orcid.org/0000-0001-7549-2124](https://orcid.org/0000-0001-7549-2124)

**Lorenzo Sorace** – Dipartimento di Chimica “Ugo Schiff” - DICUS, Università degli Studi di Firenze, I-50019 Sesto Fiorentino, Firenze, Italy; Consorzio Interuniversitario Nazionale di Scienza e Tecnologia dei Materiali - INSTM, I-50121 Firenze, Italy; [orcid.org/0000-0003-4785-1331](https://orcid.org/0000-0003-4785-1331)

Complete contact information is available at: <https://pubs.acs.org/10.1021/jacsau.3c00121>

### Author Contributions

CRedit: **Fabio Santanni** conceptualization, formal analysis, investigation, writing-original draft, writing-review & editing; **Matteo Briganti** formal analysis, funding acquisition, investigation, writing-original draft, writing-review & editing; **Giulia Serrano** formal analysis, investigation, writing-original draft, writing-review & editing; **Enrico Salvadori** formal analysis, investigation, writing-review & editing; **Alessandro Veneri** formal analysis, investigation, writing-original draft; **Chiara Batistoni** investigation; **Sofia Frida Russi** investigation; **Stefano Menichetti** supervision, writing-review & editing; **Matteo Mannini** formal analysis, funding acquisition, supervision, writing-review & editing; **Mario Chiesa** investigation, supervision, writing-review & editing; **Lorenzo Sorace** supervision, writing-review & editing; **Roberta Sessoli** conceptualization, funding acquisition, supervision, writing-original draft, writing-review & editing.

### Notes

The authors declare no competing financial interest.

### ACKNOWLEDGMENTS

The support of EC through the EU Commission through the FETOPEN project FATMOLS (GA 862893) and Italian MIUR through Progetto Dipartimenti di Eccellenza 2023–2027 (DICUS 2.0) to the Department of Chemistry “Ugo Schiff” of the University of Florence and PNRR MUR project PE0000023-NQSTI is acknowledged. A.V. gratefully acknowledges MUR and EU-FSE for the financial support of the PhD fellowship PON Research and Innovation 2014–2020 (D.M. 1061/2021). M.B. thanks Fondazione Cassa di Risparmio di Firenze for the “Giovani Ricercatori Protagonisti” fellowship. We acknowledge the support of Dr. S. Ciattini, Dr. L. Chelazzi, and Dr. E. Fantechi (CRIST—University of Florence) for the crystallographic data analysis, Prof. M. Severi (Univ. of Florence) for ICP-AES measurements, and the MatchLab Interdepartment Research Unit (Univ. of Florence). Dr. Yu-Kai Liao is gratefully acknowledged for performing the spin diffusion experiments.

### REFERENCES

- (1) Morello, A.; Pla, J. J.; Bertet, P.; Jamieson, D. N. Donor Spins in Silicon for Quantum Technologies. *Adv. Quantum Technol.* **2020**, *3*, No. 2000005.
- (2) Atzori, M.; Sessoli, R. The Second Quantum Revolution: Role and Challenges of Molecular Chemistry. *J. Am. Chem. Soc.* **2019**, *141*, 11339–11352.
- (3) Heinrich, A. J.; Oliver, W. D.; Vandersypen, L. M. K.; Ardavan, A.; Sessoli, R.; Loss, D.; Jayich, A. B.; Fernandez-Rossier, J.; Laucht, A.; Morello, A. Quantum-Coherent Nanoscience. *Nat. Nanotechnol.* **2021**, *16*, 1318–1329.
- (4) Warren, A.; Economou, S. E. Silicon Qubits Move a Step Closer to Achieving Error Correction. *Nature* **2022**, *601*, 320–322.
- (5) Macaluso, E.; Rubín, M.; Aguilà, D.; Chiesa, A.; Barrios, L. A.; Martínez, J. I.; Alonso, P. J.; Roubeau, O.; Luis, F.; Aromí, G.; Carretta, S. A Heterometallic [LnLn'Ln] Lanthanide Complex as a

- Qubit with Embedded Quantum Error Correction. *Chem. Sci.* **2020**, *11*, 10337–10343.
- (6) Chicco, S.; Chiesa, A.; Allodi, G.; Garlatti, E.; Atzori, M.; Sorace, L.; De Renzi, R.; Sessoli, R.; Carretta, S. Controlled Coherent Dynamics of [VO(TPP)], a Prototype Molecular Nuclear Qudit with an Electronic Ancilla. *Chem. Sci.* **2021**, *12*, 12046–12055.
- (7) Chiesa, A.; Macaluso, E.; Petiziol, F.; Wimberger, S.; Santini, P.; Carretta, S. Molecular Nanomagnets as Qubits with Embedded Quantum-Error Correction. *J. Phys. Chem. Lett.* **2020**, *11*, 8610–8615.
- (8) Lockyer, S. J.; Chiesa, A.; Timco, G. A.; McInnes, E. J. L.; Bennett, T. S.; Vitorica-Yrezabal, I. J.; Carretta, S.; Winpenny, R. E. P. Targeting Molecular Quantum Memory with Embedded Error Correction. *Chem. Sci.* **2021**, *12*, 9104–9113.
- (9) Jacobberger, R. M.; Qiu, Y.; Williams, M. L.; Krzyaniak, M. D.; Wasielewski, M. R. Using Molecular Design to Enhance the Coherence Time of Quintet Multiexcitons Generated by Singlet Fission in Single Crystals. *J. Am. Chem. Soc.* **2022**, *144*, 2276–2283.
- (10) Graham, M. J.; Zdrozny, J. M.; Fataftah, M. S.; Freedman, D. E. Forging Solid-State Qubit Design Principles in a Molecular Furnace. *Chem. Mater.* **2017**, *29*, 1885–1897.
- (11) Von Kugelgen, S.; Krzyaniak, M. D.; Gu, M.; Puggioni, D.; Rondinelli, J. M.; Wasielewski, M. R.; Freedman, D. E. Spectral Addressability in a Modular Two Qubit System. *J. Am. Chem. Soc.* **2021**, *143*, 8069–8077.
- (12) Ferrando-Soria, J.; Moreno Pineda, E.; Chiesa, A.; Fernandez, A.; Magee, S. A.; Carretta, S.; Santini, P.; Vitorica-Yrezabal, I. J.; Tuna, F.; Timco, G. A.; et al. A Modular Design of Molecular Qubits to Implement Universal Quantum Gates. *Nat. Commun.* **2016**, *7*, No. 11377.
- (13) Ranieri, D.; Santanni, F.; Privitera, A.; Albino, A.; Salvadori, E.; Chiesa, M.; Totti, F.; Sorace, L.; Sessoli, R. An Exchange Coupled Meso – Meso Linked Vanadyl Porphyrin Dimer for Quantum Information Processing. *Chem. Sci.* **2023**, *14*, 61–69.
- (14) Pla, J. J.; Tan, K. Y.; Dehollain, J. P.; Lim, W. H.; Morton, J. J. L.; Jamieson, D. N.; Dzurak, A. S.; Morello, A. A Single-Atom Electron Spin Qubit in Silicon. *Nature* **2012**, *489*, 541–545.
- (15) Muhonen, J. T.; Dehollain, J. P.; Laucht, A.; Hudson, F. E.; Kalra, R.; Sekiguchi, T.; Itoh, K. M.; Jamieson, D. N.; McCallum, J. C.; Dzurak, A. S.; Morello, A. Storing Quantum Information for 30 Seconds in a Nanoelectronic Device. *Nat. Nanotechnol.* **2014**, *9*, 986–991.
- (16) Kobayashi, T.; Salfi, J.; Chua, C.; van der Heijden, J.; House, M. G.; Culcer, D.; Hutchison, W. D.; Johnson, B. C.; McCallum, J. C.; Riemann, H.; Abrosimov, N. V.; Becker, P.; Pohl, H.; Simmons, M. Y.; Rogge, S. Engineering Long Spin Coherence Times of Spin–Orbit Qubits in Silicon. *Nat. Mater.* **2021**, *20*, 38–42.
- (17) Bader, K.; Dengler, D.; Lenz, S.; Endeward, B.; Jiang, S.-D.; Neugebauer, P.; van Slageren, J. Room Temperature Quantum Coherence in a Potential Molecular Qubit. *Nat. Commun.* **2014**, *5*, No. 5304.
- (18) Zdrozny, J. M.; Niklas, J.; Poluektov, O. G.; Freedman, D. E. Millisecond Coherence Time in a Tunable Molecular Electronic Spin Qubit. *ACS Cent. Sci.* **2015**, *1*, 488–492.
- (19) Graham, M. J.; Yu, C.-J.; Krzyaniak, M. D.; Wasielewski, M. R.; Freedman, D. E. Synthetic Approach To Determine the Effect of Nuclear Spin Distance on Electronic Spin Decoherence. *J. Am. Chem. Soc.* **2017**, *139*, 3196–3201.
- (20) Canarie, E. R.; Jahn, S. M.; Stoll, S. Quantitative Structure-Based Prediction of Electron Spin Decoherence in Organic Radicals. *J. Phys. Chem. Lett.* **2020**, *11*, 3396–3400.
- (21) Santanni, F.; Albino, A.; Atzori, M.; Ranieri, D.; Salvadori, E.; Chiesa, M.; Lunghi, A.; Bencini, A.; Sorace, L.; Totti, F.; Sessoli, R. Probing Vibrational Symmetry Effects and Nuclear Spin Economy Principles in Molecular Spin Qubits. *Inorg. Chem.* **2021**, *60*, 140–151.
- (22) Escalera-Moreno, L.; Gaita-Ariño, A.; Coronado, E. Decoherence from Dipolar Interspin Interactions in Molecular Spin Qubits. *Phys. Rev. B* **2019**, *100*, No. 064405.
- (23) Atzori, M.; Morra, E.; Tesi, L.; Albino, A.; Chiesa, M.; Sorace, L.; Sessoli, R. Quantum Coherence Times Enhancement in Vanadium(IV)-Based Potential Molecular Qubits: The Key Role of the Vanadyl Moiety. *J. Am. Chem. Soc.* **2016**, *138*, 11234–11244.
- (24) Chen, J.; Hu, C.; Stanton, J. F.; Hill, S.; Cheng, H.-P.; Zhang, X.-G. Decoherence in Molecular Electron Spin Qubits: Insights from Quantum Many-Body Simulations. *J. Phys. Chem. Lett.* **2020**, *11*, 2074–2078.
- (25) Lin, C.-Y.; Ngendahimana, T.; Eaton, G. R.; Eaton, S. S.; Zdrozny, J. M. Counterion Influence on Dynamic Spin Properties in a  $V^{IV}$  Complex. *Chem. Sci.* **2019**, *10*, 548–555.
- (26) Jackson, C. E.; Ngendahimana, T.; Lin, C.-Y.; Eaton, G. R.; Eaton, S. S.; Zdrozny, J. M. Impact of Counter Ion Methyl Groups on Spin Relaxation in  $[V(C_6H_4O_2)_3]^{2-}$ . *J. Phys. Chem. C* **2022**, *126*, 7169–7176.
- (27) Sorrentino, A. L.; Cimatti, I.; Serrano, G.; Poggini, L.; Cortigiani, B.; Malavolti, L.; Otero, E.; Sainctavit, P.; Mannini, M.; Sessoli, R.; Caneschi, A. A TbPc<sub>2</sub> Sub-Monolayer Deposit on a Titanium Dioxide Ultrathin Film: Magnetic, Morphological, and Chemical Insights. *J. Mater. Chem. C* **2021**, *9*, 15011–15017.
- (28) Serrano, G.; Poggini, L.; Cucinotta, G.; Sorrentino, A. L.; Giaconi, N.; Cortigiani, B.; Longo, D.; Otero, E.; Sainctavit, P.; Caneschi, A.; Mannini, M.; Sessoli, R. Magnetic Molecules as Local Sensors of Topological Hysteresis of Superconductors. *Nat. Commun.* **2022**, *13*, No. 3838.
- (29) Godfrin, C.; Ferhat, A.; Ballou, R.; Klyatskaya, S.; Ruben, M.; Wernsdorfer, W.; Balestro, F. Operating Quantum States in Single Magnetic Molecules: Implementation of Grover's Quantum Algorithm. *Phys. Rev. Lett.* **2017**, *119*, No. 187702.
- (30) Manassen, Y.; Averbukh, M.; Jbara, M.; Siebenhofer, B.; Shnirman, A.; Horovitz, B. Fingerprints of Single Nuclear Spin Energy Levels Using STM – ENDOR. *J. Magn. Reson.* **2018**, *289*, 107–112.
- (31) Zhang, X.; Wolf, C.; Wang, Y.; Aubin, H.; Bilgeri, T.; Willke, P.; Heinrich, A. J.; Choi, T. Electron Spin Resonance of Single Iron Phthalocyanine Molecules and Role of Their Non-Localized Spins in Magnetic Interactions. *Nat. Chem.* **2022**, *14*, 59–65.
- (32) Willke, P.; Bilgeri, T.; Zhang, X.; Wang, Y.; Wolf, C.; Aubin, H.; Heinrich, A.; Choi, T. Coherent Spin Control of Single Molecules on a Surface. *ACS Nano* **2021**, *15*, 17959–17965.
- (33) Serrano, G.; Poggini, L.; Briganti, M.; Sorrentino, A. L.; Cucinotta, G.; Malavolti, L.; Cortigiani, B.; Otero, E.; Sainctavit, P.; Loth, S.; Parenti, F.; Barra, A. L.; Vindigni, A.; Cornia, A.; Totti, F.; Mannini, M.; Sessoli, R. Quantum Dynamics of a Single Molecule Magnet on Superconducting Pb(111). *Nat. Mater.* **2020**, *19*, 546–551.
- (34) *Dithiolene Chemistry*, Stiefel, E. I., Ed.; Progress in Inorganic Chemistry vol. 52. John Wiley & Sons, Inc.: Hoboken, NJ, USA, 2003.
- (35) Zhou, B.; Yajima, H.; Kobayashi, A.; Okano, Y.; Tanaka, H.; Kumashiro, T.; Nishibori, E.; Sawa, H.; Kobayashi, H. Single-Component Molecular Conductor  $[Cu(Tmdt)_2]$  Containing an Antiferromagnetic Heisenberg Chain. *Inorg. Chem.* **2010**, *49*, 6740–6747.
- (36) Nakamura, T.; Sasamori, K.; Kodama, T.; Kikuchi, K.; Fujita, W. Preparation, Crystal Structure, and Magnetic Properties of a New Dithiolene Ligand, 1,3,2-Dithiazole-4-Thione-5-Thiolate, and Its Metal Complex. *Chem. - Asian J.* **2013**, *8*, 348–350.
- (37) Morris, J. L.; Rees, C. W.; Rigg, D. J. 1,3,5,2,4-Trithiadiazepine. *J. Chem. Soc. Chem. Commun.* **1985**, *7*, 396.
- (38) Morris, J. L.; Rees, C. W. Organic Heterocyclothiazenes. Part 3. Synthesis and Structure of 1,3,5,2,4-Trithiadiazepines. *J. Chem. Soc., Perkin Trans. 1* **1987**, 211–215.
- (39) Johann, R.; Wolmershäuser, G. 1,3,2-Dithiazolylium Cations with Various Anions; Syntheses and Solid State Structures. *Phosphorus. Silicon Relat. Elem.* **1997**, *124*, 233–242.
- (40) Biesinger, M. C. Advanced Analysis of Copper X-Ray Photoelectron Spectra. *Surf. Interface Anal.* **2017**, *49*, 1325–1334.
- (41) Healy, P. C.; Myhra, S.; Stewart, A. M. XPS Studies of Planar Four-Coordinate Copper(II) and Copper(III) Complexes. *Jpn. J. Appl. Phys.* **1987**, *26*, L1884–L1887.
- (42) Ivanova, T. M.; Maslakov, K. I.; Sidorov, A. A.; Kiskin, M. A.; Linko, R. V.; Savilov, S. V.; Lunin, V. V.; Eremenko, I. L. XPS

Detection of Unusual Cu(II) to Cu(I) Transition on the Surface of Complexes with Redox-Active Ligands. *J. Electron Spectros. Relat. Phenomena* **2020**, *238*, No. 146878.

(43) Singh, V.; Kim, J.; Kang, B.; Moon, J.; Kim, S.; Kim, W. Y.; Byon, H. R. Thiazole-Linked Covalent Organic Framework Promoting Fast Two-Electron Transfer for Lithium-Organic Batteries. *Adv. Energy Mater.* **2021**, *11*, No. 2003735.

(44) Wang, Y.; Im, J.; Soares, J. W.; Steeves, D. M.; Whitten, J. E. Thiol Adsorption on and Reduction of Copper Oxide Particles and Surfaces. *Langmuir* **2016**, *32*, 3848–3857.

(45) Qie, L.; Chen, W.; Xiong, X.; Hu, C.; Zou, F.; Hu, P.; Huang, Y. Sulfur-Doped Carbon with Enlarged Interlayer Distance as a High-Performance Anode Material for Sodium-Ion Batteries. *Adv. Sci.* **2015**, *2*, DOI: 10.1002/advs.2015001951500195.

(46) Wang, Z.; Dong, Y.; Li, H.; Zhao, Z.; Bin Wu, H.; Hao, C.; Liu, S.; Qiu, J.; Lou, X. W. Enhancing Lithium–Sulphur Battery Performance by Strongly Binding the Discharge Products on Amino-Functionalized Reduced Graphene Oxide. *Nat. Commun.* **2014**, *5*, No. 5002.

(47) Sun, C.; Zhang, Y.; Wang, P.; Yang, Y.; Wang, Y.; Xu, J.; Wang, Y.; Yu, W. W. Synthesis of Nitrogen and Sulfur Co-Doped Carbon Dots from Garlic for Selective Detection of Fe<sup>3+</sup>. *Nanoscale Res. Lett.* **2016**, *11*, 110.

(48) Obrosova, A.; Gulyaev, R.; Ratzke, M.; Volinsky, A.; Bolz, S.; Naveed, M.; Weiß, S. XPS and AFM Investigations of Ti-Al-N Coatings Fabricated Using DC Magnetron Sputtering at Various Nitrogen Flow Rates and Deposition Temperatures. *Metals* **2017**, *7*, 52.

(49) Karweik, D. H.; Winograd, N. Nitrogen Charge Distributions in Free-Base Porphyrins, Metalloporphyrins, and Their Reduced Analogs Observed by X-Ray Photoelectron Spectroscopy. *Inorg. Chem.* **1976**, *15*, 2336–2342.

(50) Prieto, P.; Kirby, R. E. X-ray Photoelectron Spectroscopy Study of the Difference between Reactively Evaporated and Direct Sputter-deposited TiN Films and Their Oxidation Properties. *J. Vac. Sci. Technol. A Vacuum, Surfaces, Film.* **1995**, *13*, 2819–2826.

(51) Zeng, D. W.; Yung, K. C.; Xie, C. S. XPS Investigation of the Chemical Characteristics of Kapton Films Ablated by a Pulsed TEA CO<sub>2</sub> Laser. *Surf. Coatings Technol.* **2002**, *153*, 210–216.

(52) Wang, P. S.; Sen, Wittberg, T. N.; Wolf, J. D. A Characterization of Kapton Polyimide by X-Ray Photoelectron Spectroscopy and Energy Dispersive Spectroscopy. *J. Mater. Sci.* **1988**, *23*, 3987–3991.

(53) Zhou, B.; Idobata, Y.; Kobayashi, A.; Cui, H.; Kato, R.; Takagi, R.; Miyagawa, K.; Kanoda, K.; Kobayashi, H. Single-Component Molecular Conductor [Cu(Dmdt)<sub>2</sub>] with Three-Dimensionally Arranged Magnetic Moments Exhibiting a Coupled Electric and Magnetic Transition. *J. Am. Chem. Soc.* **2012**, *134*, 12724–12731.

(54) Noma, H.; Ohara, K.; Naito, T. Direct Control of Spin Distribution and Anisotropy in Cu-Dithiolene Complex Anions by Light. *Inorganics* **2016**, *4*, 7.

(55) Baker, E. N.; Norris, G. E. Copper Coordination to Thioether Ligands: Crystal and Molecular Structures of Bis(2,5-Dithiahexane)-Copper(II) Bis(Tetrafluoroborate) and Bis(3,6-Dithiaoctane)-Copper(I) Tetrafluoroborates. *J. Chem. Soc. Dalton Trans.* **1977**, *9*, 877.

(56) Suzuki, Y.; Fujimori, M.; Yoshikawa, H.; Awaga, K. Packing Motifs and Magneto-Structural Correlations in Crystal Structures of Metallo-Tetrakis(1,2,5-Thiadiazole)Porphyrine Series, MTTDPz (M=H<sub>2</sub>, Fe, Co, Ni, Cu, Zn). *Chem. - Eur. J.* **2004**, *10*, 5158–5164.

(57) Kahn, O. *Molecular Magnetism*; VCH Publishers, Inc.: New York NY, 1993.

(58) Bonner, J. C.; Fisher, M. E. Linear Magnetic Chains with Anisotropic Coupling. *Phys. Rev.* **1964**, *135*, A640–A658.

(59) Ruthstein, S.; Artzi, R.; Goldfarb, D.; Naaman, R. EPR Studies on the Organization of Self-Assembled Spin-Labeled Organic Monolayers Adsorbed on GaAs. *Phys. Chem. Chem. Phys.* **2005**, *7*, 524.

(60) Hoffmann, S. K.; Goslar, J.; Lijewski, S.; Zalewska, A. EPR and ESE of CuS<sub>4</sub> Complex in Cu(Dmit)<sub>2</sub>: G-Factor and Hyperfine Splitting Correlation in Tetrahedral Cu–Sulfur Complexes. *J. Magn. Reson.* **2013**, *236*, 7–14.

(61) Stoll, S.; Schweiger, A. EasySpin, a Comprehensive Software Package for Spectral Simulation and Analysis in EPR. *J. Magn. Reson.* **2006**, *178*, 42–55.

(62) Ritterskamp, N.; Sharples, K.; Richards, E.; Folli, A.; Chiesa, M.; Platts, J. A.; Murphy, D. M. Understanding the Coordination Modes of [Cu(Acac)<sub>2</sub>(Imidazole)<sub>n = 1,2</sub>] Adducts by EPR, ENDOR, HYSCORE, and DFT Analysis. *Inorg. Chem.* **2017**, *56*, 11862–11875.

(63) Penfield, K. W.; Gay, R. R.; Himmelwright, R. S.; Eickman, N. C.; Norris, V. A.; Freeman, H. C.; Solomon, E. I. Spectroscopic Studies on Plastocyanin Single Crystals: A Detailed Electronic Structure Determination of the Blue Copper Active Site. *J. Am. Chem. Soc.* **1981**, *103*, 4382–4388.

(64) Vance, C. T.; Welch, J. H.; Bereman, R. D. Syntheses, Characterization and Structural Studies of Copper Complexes of the 1,2-Dithiolene Ligand, 5,6-Dihydro-1,4-Dithiin-2,3-Dithiolate. *Inorg. Chim. Acta* **1989**, *164*, 191–200.

(65) Eaton, S. S.; Eaton, G. R. Relaxation Times of Organic Radicals and Transition Metal Ions. In *Distance Measurements in Biological Systems by EPR*, Berliner, L. J.; Eaton, G. R.; Eaton, S. S., Eds.; Kluwer Academic Publishers, 2002; pp 29–154 DOI: 10.1007/0-306-47109-4\_2.

(66) Atzori, M.; Tesi, L.; Morra, E.; Chiesa, M.; Sorace, L.; Sessoli, R. Room-Temperature Quantum Coherence and Rabi Oscillations in Vanadyl Phthalocyanine: Toward Multifunctional Molecular Spin Qubits. *J. Am. Chem. Soc.* **2016**, *138*, 2154–2157.

(67) Warner, M.; Din, S.; Tupitsyn, I. S.; Morley, G. W.; Stoneham, A. M.; Gardener, J. A.; Wu, Z.; Fisher, A. J.; Heutz, S.; Kay, C. W. M.; Aepli, K. Potential for Spin-Based Information Processing in a Thin-Film Molecular Semiconductor. *Nature* **2013**, *503*, 504–508.

(68) Lunghi, A.; Sanvito, S. The Limit of Spin Lifetime in Solid-State Electronic Spins. *J. Phys. Chem. Lett.* **2020**, *11*, 6273–6278.

(69) Du, J.-L.; Eaton, G. R.; Eaton, S. S. Electron Spin Relaxation in Vanadyl, Copper(II), and Silver(II) Porphyrins in Glassy Solvents and Doped Solids. *J. Magn. Reson. Ser. A* **1996**, *119*, 240–246.

(70) Zhuang, X.-M.; Liang, Y.-W.; Zuo, H.-R.; Huang, Q.; Yu, L.-L.; Yang, L.-M.; Ni, C.-L. Synthesis, Crystal Structure, Weak Interactions, Spectra and Magnetic Behavior of a New Ion-Pair Complex Containing Bis(Maleonitriledithiolato)Nickel(III) Monoanion and Substituted Isoquinolinium Cation. *Synth. React. Inorganic, Met. Nano-Metal Chem.* **2009**, *39*, 388–393.

(71) Salikhov, K.; Dzuba, S.; Raitisimring, A. The Theory of Electron Spin-Echo Signal Decay Resulting from Dipole-Dipole Interactions between Paramagnetic Centers in Solids. *J. Magn. Reson.* **1981**, *42*, 255–276.

(72) Camargo, L. C.; Briganti, M.; Santana, F. S.; Stingham, D.; Ribeiro, R. R.; Nunes, G. G.; Soares, J. F.; Salvadori, E.; Chiesa, M.; Benci, S.; Torre, R.; Sorace, L.; Totti, F.; Sessoli, R. Exploring the Organometallic Route to Molecular Spin Qubits: The [CpTi(Cot)] Case. *Angew. Chem., Int. Ed.* **2021**, *60*, 2588–2593.

(73) Salikhov, K. M.; Tsvetkov, Y. D. Electron Spin-Echo Studies of Spin–Spin Interactions in Solids. In *Time Domain Electron Spin Resonance*, Kevan, L.; Schwartz, R. N., Eds.; Wiley-Interscience: New York, 1979; pp 231–277.

(74) Tyryshkin, A. M.; Tojo, S.; Morton, J. J. L.; Riemann, H.; Abrosimov, N. V.; Becker, P.; Pohl, H.-J.; Schenkel, T.; Thewalt, M. L. W.; Itoh, K. M.; Lyon, S. A. Electron Spin Coherence Exceeding Seconds in High-Purity Silicon. *Nat. Mater.* **2012**, *11*, 143–147.

(75) Barr, T. L.; Seal, S. Nature of the Use of Adventitious Carbon as a Binding Energy Standard. *J. Vac. Sci. Technol. A Vacuum, Surfaces, Films* **1995**, *13*, 1239–1246.

(76) Yeh, J. J.; Lindau, I. Atomic Subshell Photoionization Cross Sections and Asymmetry Parameters: 1 ≤ Z ≤ 103. *At. Data Nucl. Data Tables* **1985**, *32*, 1–155.

(77) Dolomanov, O. V.; Bourhis, L. J.; Gildea, R. J.; Howard, J. A. K.; Puschmann, H. OLEX2: A Complete Structure Solution,

Refinement and Analysis Program. *J. Appl. Crystallogr.* **2009**, *42*, 339–341.

(78) Sheldrick, G. M. SHELXT – Integrated Space-Group and Crystal-Structure Determination. *Acta Crystallogr. Sect. A Found. Adv.* **2015**, *71*, 3–8.

(79) Sheldrick, G. M. A Short History of SHELX. *Acta Crystallogr., Sect. A: Found. Crystallogr.* **2008**, *64*, 112–122.

(80) Macrae, C. F.; Sovago, I.; Cottrell, S. J.; Galek, P. T. A.; McCabe, P.; Pidcock, E.; Platings, M.; Shields, G. P.; Stevens, J. S.; Towler, M.; Wood, P. A. Mercury 4.0: From Visualization to Analysis, Design and Prediction. *J. Appl. Crystallogr.* **2020**, *53*, 226–235.

(81) Bain, G. A.; Berry, J. F. Diamagnetic Corrections and Pascal's Constants. *J. Chem. Educ.* **2008**, *85*, 532.

(82) Neese, F.; Wennmohs, F.; Becker, U.; Riplinger, C. The ORCA Quantum Chemistry Program Package. *J. Chem. Phys.* **2020**, *152*, No. 224108.

(83) Adamo, C.; Barone, V. Toward Reliable Density Functional Methods without Adjustable Parameters: The PBE0 Model. *J. Chem. Phys.* **1999**, *110*, 6158–6170.

(84) Weigend, F.; Ahlrichs, R. Balanced Basis Sets of Split Valence, Triple Zeta Valence and Quadruple Zeta Valence Quality for H to Rn: Design and Assessment of Accuracy. *Phys. Chem. Chem. Phys.* **2005**, *7*, 3297.

(85) Bencini, A.; Totti, F. A Few Comments on the Application of Density Functional Theory to the Calculation of the Magnetic Structure of Oligo-Nuclear Transition Metal Clusters. *J. Chem. Theory Comput.* **2009**, *5*, 144–154.

(86) Yamaguchi, K.; Takahara, Y.; Fueno, T. Ab-Initio Molecular Orbital Studies of Structure and Reactivity of Transition Metal-OXO Compounds. In *Applied Quantum Chemistry*, Springer: Netherlands: Dordrecht, 1986; pp 155–184.

(87) Hedegård, E. D.; Kongsted, J.; Sauer, S. P. A. Optimized Basis Sets for Calculation of Electron Paramagnetic Resonance Hyperfine Coupling Constants: Aug-Cc-PVTZ-J for the 3d Atoms Sc–Zn. *J. Chem. Theory Comput.* **2011**, *7*, 4077–4087.

(88) Neese, F.; Wennmohs, F.; Hansen, A.; Becker, U. Efficient, Approximate and Parallel Hartree–Fock and Hybrid DFT Calculations. A 'Chain-of-Spheres' Algorithm for the Hartree–Fock Exchange. *Chem. Phys.* **2009**, *356*, 98–109.

(89) Stamp, P. C.; Tupitsyn, I. Crossovers in Spin-Boson and Central Spin Models. *Chem. Phys.* **2004**, *296*, 281–293.

(90) Höfer, P.; Grupp, A.; Nebenführ, H.; Mehring, M. Hyperfine Sublevel Correlation (Hyscore) Spectroscopy: A 2D ESR Investigation of the Squaric Acid Radical. *Chem. Phys. Lett.* **1986**, *132*, 279–282.